ORIGINAL ARTICLE

Effect of crystallinity and particle size on coke-based anode for lithium ion batteries

Seung Eun Lee[1,2] · Ji Hong Kim[1,3] · Young-Seak Lee[2] · Byong Chol Bai[4] · Ji Sun Im[1,5]

Abstract

This study examined the effects of micro- (crystallinity) and macro (orientation)-crystalline properties of graphite on the initial efficiency, discharge capacity, and rate performance of anodic materials. Needle coke and regular coke were selected as raw materials and pulverized to 2–25 μm to determine the effects of crystalline properties on particle shape after pulverization. Needle coke with outstanding crystallinity had high initial efficiency, and smaller particles with larger specific surface areas saw increased irreversible capacity due to the formation of SEI layers. Because of cavities existing between crystals, the poorer the crystalline properties were, the greater the capacity of the lithium ions increased. As such, regular coke had a 30 mAh/g higher discharge capacity than that of needle coke. Rate performance was more affected by particle size than by crystalline structure, and was the highest at a particle distribution of 10–15 μm.

Keywords Needle coke · Regular coke · Crystallinity · Particle size · Lithium ion batteries

1 Introduction

With the recent emergence of environmental/energy issues, there has been a growing demand for medium/large-sized secondary batteries, which are used as sources of power for electric vehicles (EV) and hybrid electric vehicles (HEV). Extensive research is being conducted on lithium secondary batteries, focusing on aspects, such as large capacity, battery life, and high output. Performance improvement of lithium secondary batteries depends on four factors: cathode, anode, electrolyte, and separator. In the case of anodes, intercalation and de-intercalation of lithium ions are more difficult than cathode due to their larger capacity per unit weight. Battery design should consider lithium intercalation and de-intercalation at anodes for enhanced performance [1].

Graphite is widely used as an anode active material because of its excellent cycle stability, due to its intercalation reaction mechanism, and its affordable cost, even the capacity is very poor. However, graphite is pulverized to flake shape, so the orientation is parallel to the current collector during the casting and rolling process [2, 3]. This orientation reduces the active sites for charge/discharge of lithium ions in graphite, thereby deteriorating the rate performance. Anode materials having crystalline properties similar to those of graphite are more susceptible to delamination and decomposition caused by electrolyte permeation, and will see significant increases in irreversible capacity during the charge/discharge process [4–7]. A comprehensive examination of the crystallinity and shape of graphite is needed to enhance the properties of secondary batteries, including capacity, battery life, and rate performance.

The crystalline properties of graphite can be considered from micro and macro perspectives. From a micro perspective, crystalline properties of graphite are included crystal

✉ Ji Sun Im
  jsim@krict.re.kr

  Byong Chol Bai
  baibc820@kictex.re.kr

1   C1 Gas and Carbon Convergent Research Center, Korea Research Institute of Chemical Technology (KRICT), Daejeon 34114, Republic of Korea

2   Department of Chemical Engineering and Applied Chemistry, Chungnam National University, Daejeon 34134, Republic of Korea

3   Department of Chemical and Biological Engineering, Korea University, Seoul 02841, Republic of Korea

4   Korea Institute of Convergence Textile, Iksan, Jeollabuk-do 54588, Republic of Korea

5   Advanced Materials and Chemical Engineering, University of Science and Technology (UST), Daejeon 34113, Republic of Korea

size and defects, which are influenced by process conditions (temperature, pressure, etc.) during the graphitization [8–10]. From a macro perspective, crystalline structure refers to the orientation of crystals, determined by flow or external force during coking of crystals within the carbonaceous material. That is, the crystalline properties of graphite are determined by orientation during coking, and this produces anode materials with different properties. Therefore, studying the correlation between the properties of coke, such as crystallinity and particle shape, and anodes is essential in research on graphitic anode materials.

This study chose needle coke and regular coke, which have different crystallinity and orientation as raw materials, and fabricated anode materials measuring 2–25 μm to examine the effect of coke shape on electrode fabrication. From a macro perspective, the particle shape and orientations of samples were investigated through scanning electron microscopy (SEM) and polarized optical microscopy. From a micro perspective, crystalline properties were analyzed using X-ray diffraction (XRD) and Raman spectroscopy. The effects of crystalline properties at the macro and micro levels on the anodic properties of secondary batteries were examined based on a comparison of electrochemical properties, such as initial efficiency, discharge capacity, and rate performance.

2 Experiment

2.1 Fabrication of coke as anode material

This study used two coal-based cokes fabricated at the same temperature (1300 ℃) but having different textural properties. Needle coke and regular coke were named N-coke and C-coke, respectively. 250 ml of samples and a 250 ml SUS ball (size: 13/16, 5/16, 19/32, 5ø, 2ø) were placed in a 1 L bulk grinder and pulverized at 500 rpm for 120 min. The pulverized cokes were distributed at sizes of 25–15, 15–10, and 10–2 μm using a vibratory sieve shaker. The samples were named N-25, N-15, N-10, C-25, C-15, and C-10 according to their size and shape. To eliminate the effect of the functional group during pulverization, nitrogen was introduced at a rate of 100 cc/min, and reheating was performed at a rate of 5 ℃/min, starting at the fabrication temperature of 1300 ℃ (Tube Furnace, 4 L) [11, 12].

2.2 Coke crystallinity analysis

The surface shapes of particles were compared through SEM (S-2500C, Hitachi) analysis, and the orientations of fabricated cokes were examined using polarized optical microscope images. The crystallinity of samples was examined via Raman spectroscopy (LabRAM HR800) and XRD (Rigaku,

Ultima IV). XRD was performed at a current of 40 mA and voltage condition (2 kW) of 40 kW with Cu-Kα ($\lambda = 1.5418$ Å) as the light source; measurements were obtained in the range of $2° < 2\theta < 90°$ at a scanning rate of 3 ℃/min. After collecting the data with a diffractometer, data reduction was performed using the PDXL software. The interlayer distance (d) and crystal size (Lc) were calculated using Bragg's law and the Scherrer equation as provided below:

$$d = \lambda/2 \, \sin\theta \text{Bragg}, \tag{1}$$

$$\text{Lc} = K\lambda/(\beta 2\theta \cdot \cos\theta), \tag{2}$$

Lc is the aerage height of c –axis of crystal, K is the scherrer constant ($K = 0.9$), β is the radian, θ is the angle at peak.

2.3 Analysis of coke properties in relation to particle size

The shapes of pulverized samples were analyzed through SEM (S-2500C, Hitachi). Particle density was measured using a He pycnometer, and size using a particle size analyzer. A Powder Resistivity Measurement System (HPRM-M2) was employed to measure the electrical conductivity of samples. The specific surface area and pore size distribution were determined by N2 adsorption–desorption Brunauer–Emmett–Teller (BET) measurement using a Builder SSA-4200.

2.4 Electrochemical measurements

The electrochemical properties of samples were determined using constant current, constant voltage charge/discharge methods. Styrene butadiene rubber (SBR) and carboxymethyl cellulose (CMC) were used as binders for electrode fabrication, and a slurry was prepared with the sample, SBR, and CMC at a mass ratio of 95:2.5:2.5. The slurry was coated on a copper foil, which was dried in a vacuum oven for 12 h at 120 ℃. The coated electrodes were rolled in a roll presser to achieve a uniform electrode density of 1 g/cm^3. The electrode porosity was calculated as follows:

$$V_{\text{real}} = \left(W_{\text{electrode}} - W_{\text{current collector}}\right) \times \left(\frac{x_{\text{act}}}{d_{\text{act}}} + \frac{x_{\text{bd}}}{d_{\text{bd}}}\right),$$

$$V = \left(T^f_{\text{electrode}} - T_{\text{current collector}}\right) \times A_{\text{electrode}},$$

$$\text{Porosity} = \frac{V - V_{\text{real}}}{V} \times 100\%,$$

where V is the volume, T is the thickness, $T^f_{\text{electrode}}$ is th thickness after pressure, W is the weight, d is the true density, x is the ratio, act is the active material, bd is the binder.

The electrolyte was composed of 1 M LiPF$_6$/EC (ethylene carbonate) and DEC (diethyl carbonate) at a volume ratio of 1:1. A coin-type half-cell was fabricated in a glove box under an argon atmosphere with Li metal as the reference electrode. The electrochemical analysis of the battery was performed using a WBCS 3000 battery cycler (Won A Tech). Cells were charged at 0.1 C from 2.5 to 0.01 V vs. Li/Li+, followed by a constant voltage at 0.01 V. The discharge rate was measured at 0.1–5 C, and the specific capacity was assumed to 280 mAh/g. Also, we evaluated the cycling performance of the cells at 0.1 C to charge and 0.2 C to discharge. All electrochemical experiments were conducted at the same temperature of 25 °C (25 °C ± 2 °C).

## 3 Results

3.1 Texture analysis

The shapes of C-coke and N-coke were compared through FE-SEM and polarizing microscopic images, as shown in Fig. 1. In Fig. 1a and b, C-coke has a disordered amorphous structure and irregular orientation. In Fig. 1c and d,

N-coke has a well-developed layered structure, and exhibits flow texture in the axial direction.

The crystallinity of the two cokes was examined using XRD; the results are shown in Fig. 2 and Table 1. As shown in Fig. 2a, C-coke exists as a smooth curve at $2\theta = 25.52°(002)$, while N-coke (Fig. 2b) is a sharper curve at $2\theta = 26.79°(002)$. C-coke and N-coke have Lc values of 27.9 and 72.9 Å, and interlayer distance of 3.49 and 3.45 Å, which values indicate that N-coke has better crystallinity.

Raman spectroscopy was employed as shown in Fig. 3 to examine the cokes for defects. Each peak was quantified; the results are shown in Table 2. The defectiveness values (I_D/I_G) of C-coke and N-coke were 1.07 and 0.93, respectively, which translate to C-coke having a more disordered crystalline structure [13–15]. This is consistent with the apparent density values in Table 3, with N-coke having a higher density (2.17 g/ml) than that of C-coke (2.06 g/ml).

In sum, N-coke has superior orientation and higher crystallinity in the axial direction, while C-coke has a more irregular disorientation and lower crystallinity.
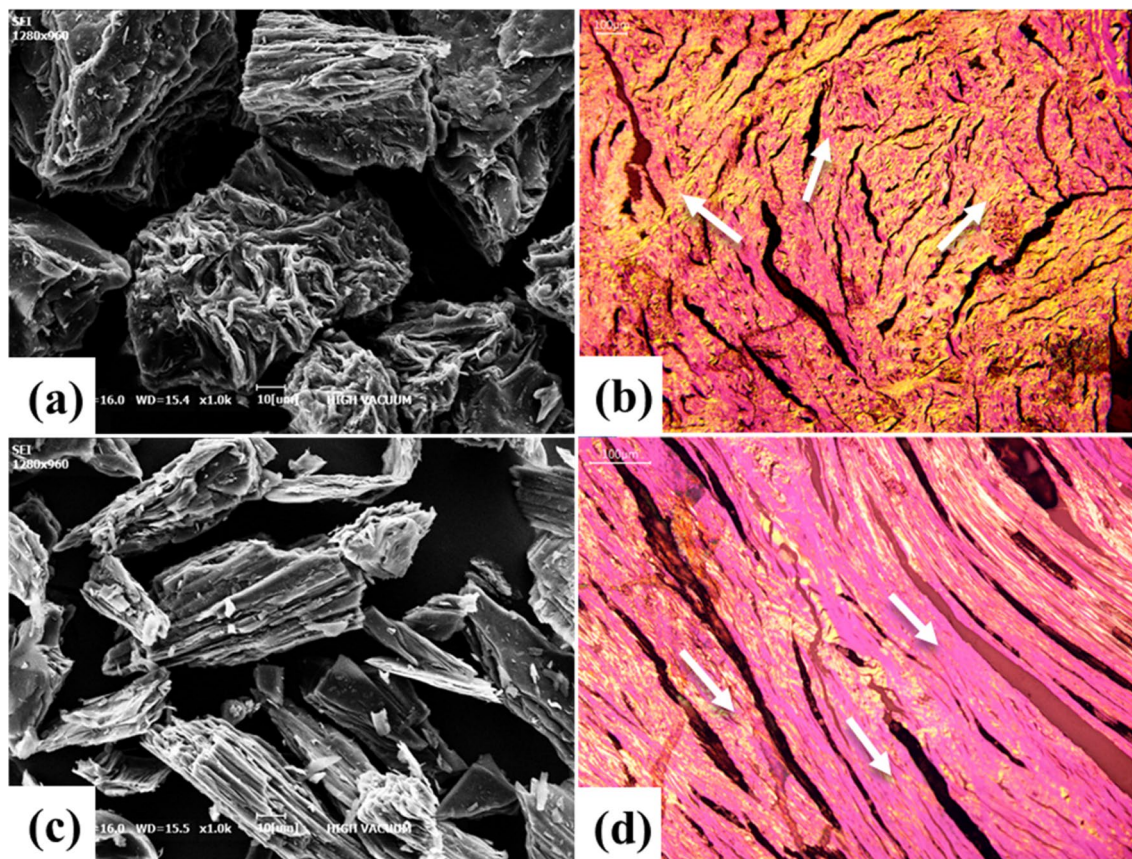
Fig. 1 SEM image of **a** C-coke, **c** N-coke and polarized optical microscopy image of **b** C-coke, **d** N-coke

Fig. 2 XRD patterns of **a** C-coke and **b** N-coke
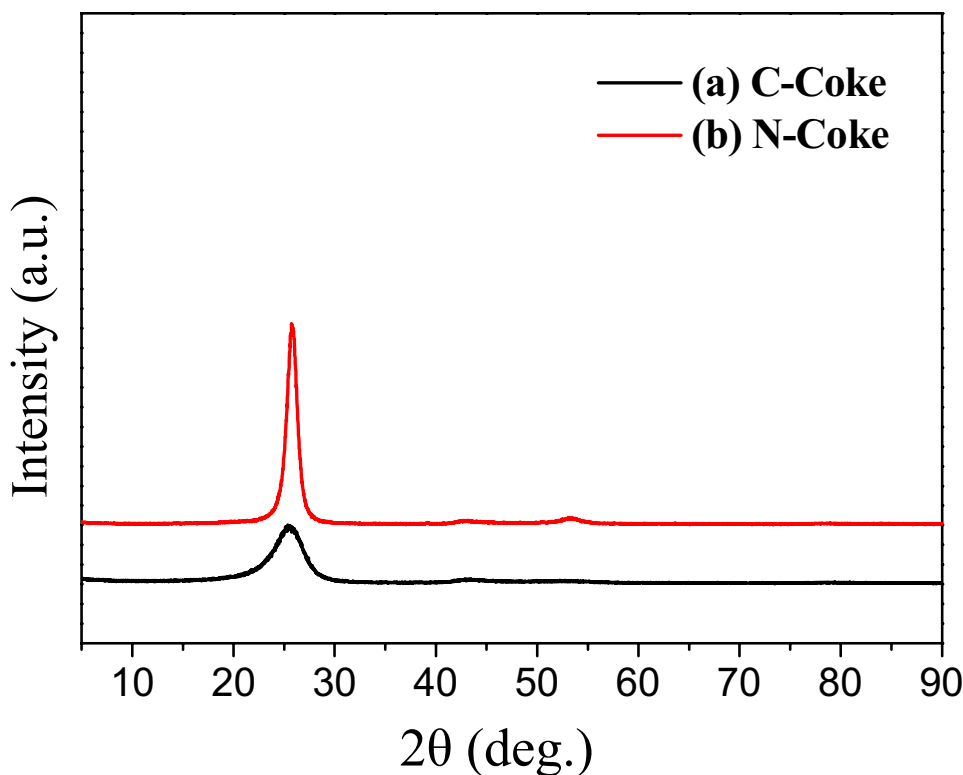
Table 1 XRD patterns of precursors

	XRD				
	d_{002}	d-spacing (Å)	FWHM	L_c (Å)	Number of layers
C-coke	25.52°	3.49	3.04	27.9	7.99
N-coke	26.79°	3.45	1.17	72.9	21.13

3.2 Analysis of physical properties in relation to particle size

The particles of pulverized cokes were examined through FE-SEM images, as shown in Fig. 4. The samples were pulverized to sizes of 25–15, 15–10, and 10–2 μm. Regular coke was named C-xxx (xxx representing particle size), and needle coke was named N-xxx. C-coke samples, which come in irregular shapes, are arranged in decreasing order of size in Fig. 4: (a) C-25, (b) C-15, and (c) C-10. N-coke has a plate-like shape and flow texture, and grows smaller in the order of (d) N-25, (e) N-15, and (f) N-10. In the previous polarizing microscopic images, C-coke showed an irregular orientation, while N-coke had flow texture in the axial direction. These crystalline properties are presumed to have influenced the pulverization process. In general, graphitic materials form strong primary bonds in the direction of the graphene layer, and weak van der Waals in the layer direction. As such, the pulverized particles assume the shape of flake [2, 3].

Particle size distribution and specific surface area are presented in Table 4. The average sizes ($D_{(50)}$) of C-25, C-15, and C-10 were 16.59, 11.20, and 6.11 μm, while those of N-25, N-15, and N-10 were 19.50, 10.18, and 6.68 μm, respectively. The specific surface areas of C-25, C-15, and C-5 were 6.06, 5.08, and 8.09 m^2/g, while those of N-25, N-15, and N-10 were 4.03, 6.35, and 7.61 m^2/g. This indicates that specific surface area increases with decreasing particle size. The increase in specific surface area was more noticeable for N-coke due to its more regular orientation. The irregular orientation of C-coke resulted in a less prominent relationship between specific surface area and particle size.

That is, C-coke with a more disordered orientation had irregular shapes, and N-coke having flow texture in the axial direction existed in plane-like shapes. For both coke types, the specific surface area increased with decreasing particle size.

3.3 Effects of shape and particle size on electrochemical properties

The initial efficiency and initial charge/discharge capacity of samples in relation to crystalline structure and particle size are shown in Table 5. The initial efficiency values of N-25, N-15, and N-10 were 88%, 86%, and 82%, while those of C-25, C-15, and C-10 were relatively lower at 82%, 81%, and 80%. In particular, N-coke (88–82%) had

Fig. 3 Raman patterns of C-coke and N-coke
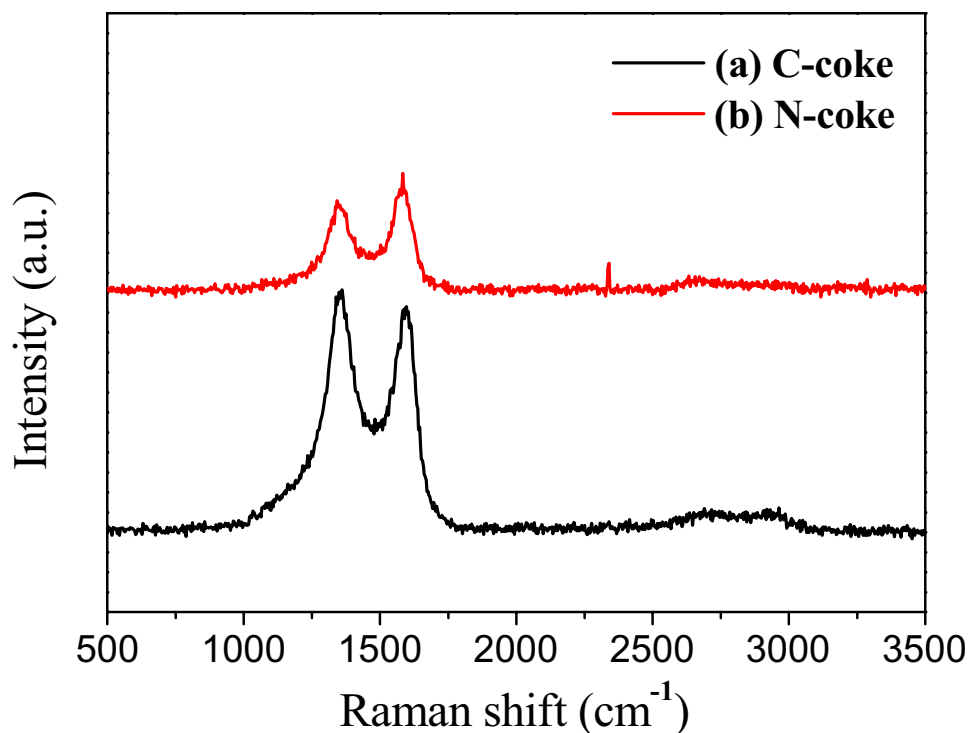
Table 2 Raman patterns of precursors

	I_D	I_G	I_D/I_G
C-coke	353	330	1.07
N-coke	465	499	0.93

Table 3 Apparent density of precursors

Name	Apparent density—He pycnometer (g/cm³)			
	6 μm	12.5 μm	20 μm	Average
C-coke	2.08	2.04	2.05	2.06
N-coke	2.16	2.18	2.17	2.17

a higher initial efficiency than that of C-coke (82–80%), which indicates that initial efficiency may be influenced by crystallinity. In general, graphitic materials with more edges will have lower initial efficiency due to their higher irreversible capacity resulting from the formation of SEI layers. SEI layers are formed when electrolyte breaks down at edges with high levels of activity. The consumption of lithium ions at this point leads to an increase in irreversible capacity. Because, compared to N-coke, irregular C-coke has a larger surface exposed for the intercalation of Li ions, it has a lower initial efficiency [10, 16]. The decrease in particle size of the two coke types caused an increase in specific surface area (increase in exposed edges), thereby lowering the initial efficiency.

The discharge capacity values of N-coke and C-coke fell in the range of 187–197 mAh/g and 205–219 mAh/g. That is, C-coke had an approximately 30 mAh/g higher discharge capacity. Discharge capacity is also influenced by the crystalline properties of materials. Generally, the lithium ion discharge mechanism in soft carbon can be divided into three types, as shown in Fig. 5 [17, 18]. Type I stores lithium ions at disordered hexagonal planes and surface sites, and has a discharge potential of 0.25–0.8 V. Type II forms LiC_6 through intercalation, and has a discharge potential of 0–0.25 V. Type III stores Li ions in the form of clusters at gaps between graphite crystals, and has a discharge potential of 0.8–2.0 V. As shown in Fig. 6, the discharge capacity of samples was divided into ranges of 0.0–0.25, 0.25–0.8, and 0.8–2.0 V.

In Table 5, the discharge capacity values of N-25, N-15, and N-10 are 187.59, 191.02, and 197.01 mAh/g. That is, discharge capacity increases with decreasing particle size. According to Fig. 6, the increase in discharge capacity is associated with the capacity attained in Type I and Type III. Type I, which involves storing lithium ions at disordered hexagonal planes and surface sites, is related to specific surface area. As reported by Yoshio et al. [10, 19–21], crystalline carbon materials see an increase in discharge capacity due to the higher number of cavities caused by surface defects at larger specific surface areas. The capacity attained under Type III increases when cavities are formed between particles due to the disordered orientation of plane-shaped particles with decreasing particle size.
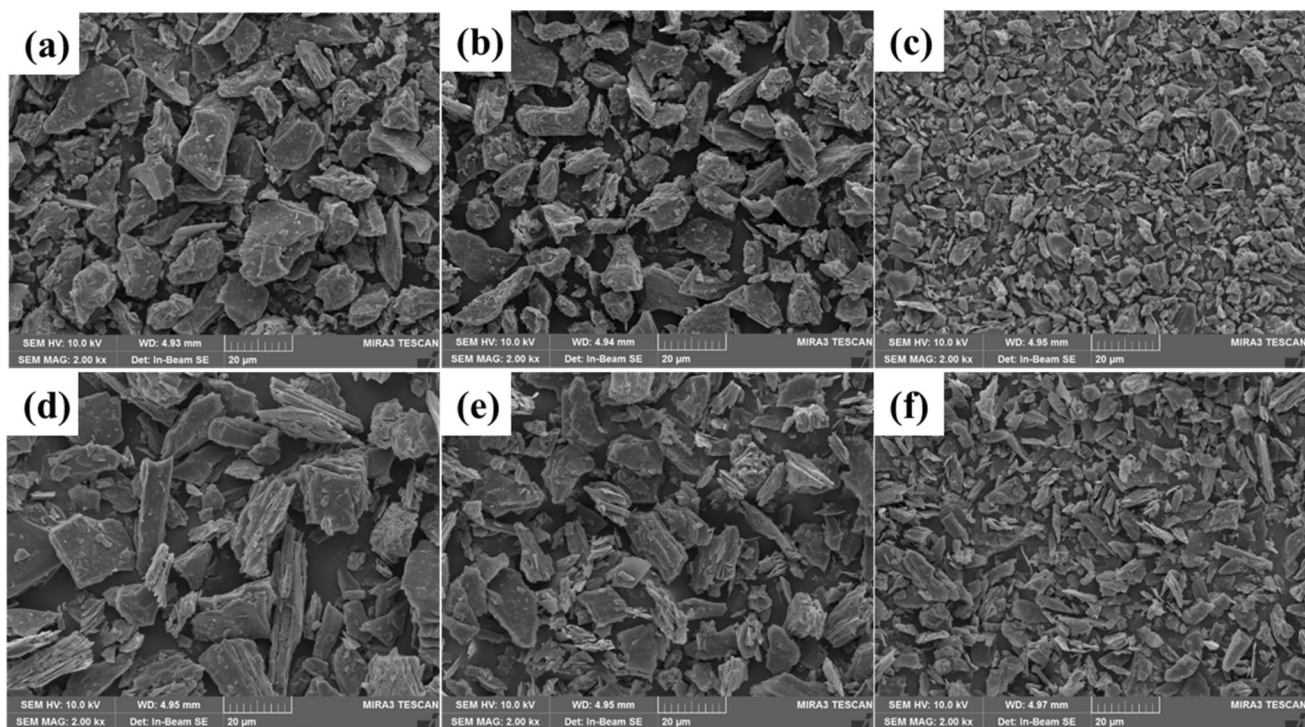
Fig. 4 SEM image of **a** C-25, **b** C-15, **c** C-10, **d** N-25, **e** N-15 and **f** N-10

Table 4 Particle size distribution data and specific surface area of prepared samples

Name	Particle size (μm)				Surface area (m²/g)
	D_{10}	D_{50}	D_{90}	FWHM	
C-25	4.21	16.59	24.57	8.30	6.06
C-15	2.86	11.20	19.97	6.29	5.08
C-10	2.76	6.11	11.67	3.37	8.08
N-25	7.45	19.50	37.89	13.48	4.03
N-15	3.30	10.18	20.96	6.71	6.35
N-10	2.81	6.68	13.04	3.78	7.61

FWHM full width at half maximum

**Table 5** Electrochemical performance of prepared samples

Name	Initial charge capacity (mAh/g)	Initial discharge capacity (mAh/g)	Coulombic efficiency (%)
C-25	267.16	219.07	82.00
C-15	266.79	217.54	81.54
C-10	256.58	205.27	80.00
N-25	212.28	187.59	88.37
N-15	221.68	191.02	86.17
N-10	238.83	197.01	82.49

On the other hand, C-coke showed a decreasing trend in discharge capacity, with values of 219.07, 217.54, and 205.27 mAh/g with smaller particle size; this reduction can be associated with Type II. In the previous XRD results, the number of graphite layers of C-coke was 7.99, which is about three times fewer than that for C-coke. The rapid decrease in number of layers with granulation is presumed to have significantly influenced Type II capacity.

As can be seen in Fig. 7a, the prepared samples have stable charge/discharge cycle properties. Rate performance in relation to crystallinity and particle size were measured and found to be 0.1, 0.2, 0.5, 1, 2, and 5 C-rate, as shown in Fig. 7; the quantified values are presented in Table 6. At 5/0.2 C, the capacity retention values were 88% and 85% for C-25 and N-25, 95% and 94% for C-15 and N-15, and identical values of 91% for C-5 and N-5. Rate performance was more affected by particle size than by crystalline structure. The factors affecting rate performance of lithium ions include electron transfer rate (electrical conductivity) and rate of diffusion of lithium ions (electrode porosity) [22, 23]. The powder resistivity of samples and electrode porosity are given in Table 7 and Fig. 8.

The electrical conductivity values of N-25, N-15, and N-10 were 91.63, 70.60, and 66.68 S/cm, which reflects a decreasing trend with smaller particle size. Similarly, the electrical conductivity values of C-coke were 41.46, 37.84,

Fig. 5 The discharge mechanism for soft carbon heat-treated at low temperatures [12, 13]
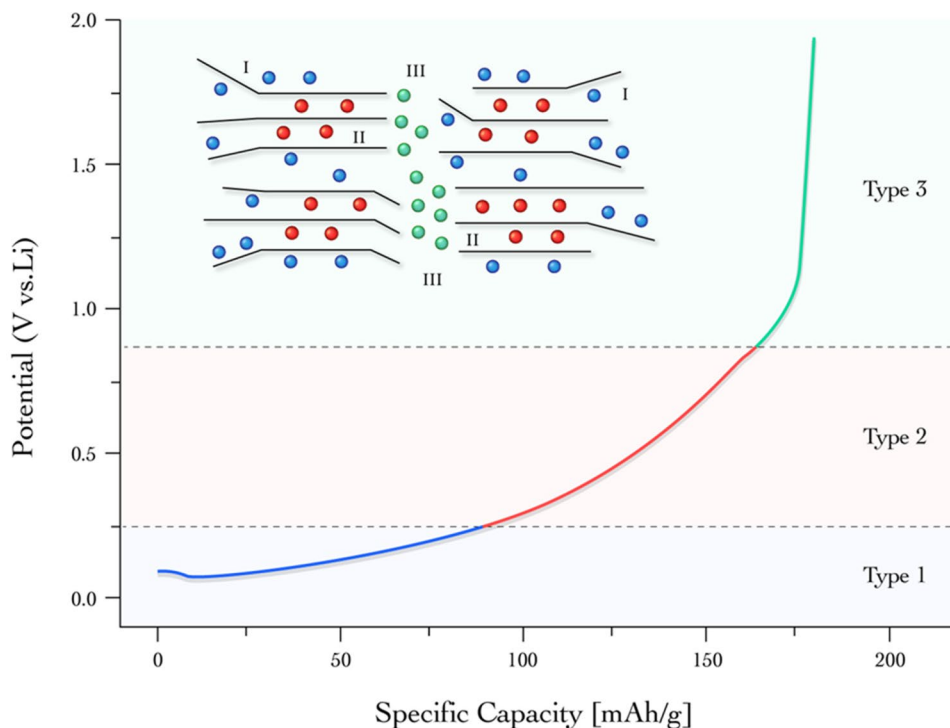

Fig. 6 Initial discharge capacity separated by the capacity mechanism
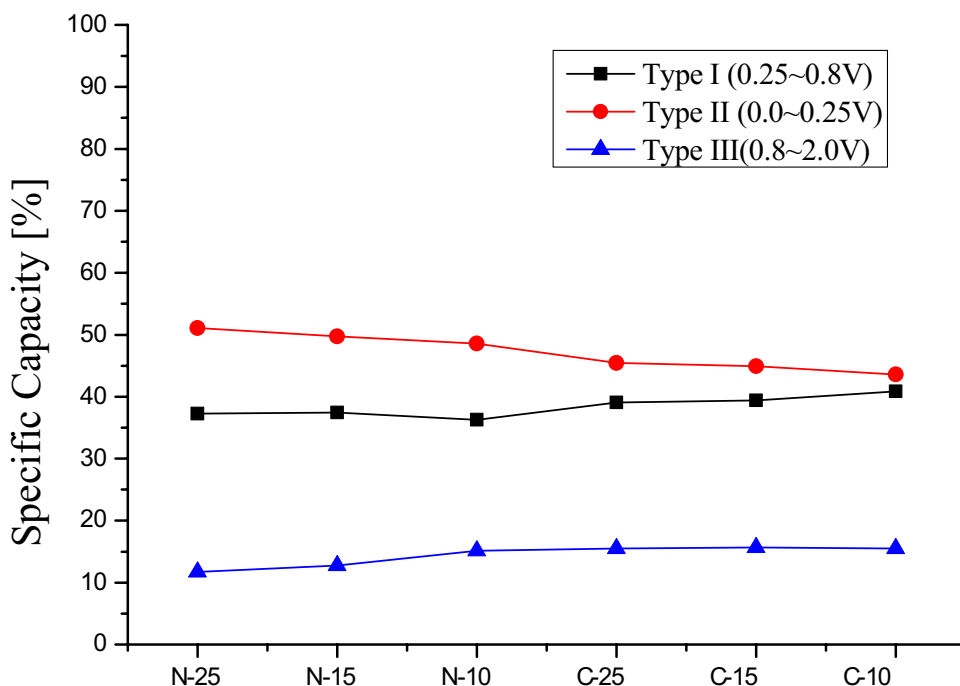
and 24.14 S/cm. This indicates an increase in contact resistance between particles with decreasing particle size. N-coke, which has superior crystallinity, had a 50 S/cm higher electrical conductivity.

All samples were designed to have an electrode density of 1 g/cm³; differences in particle size/shape and filling resulted

in different porosities. As particle size decreased from 25 to 10 μm, the porosity values of N-coke and C-coke increased from 30.76 to 41.90%, and from 35.05 to 42.68%, respectively. This is related to the particle size distribution and median diameter, shown in Table 4. Samples having smaller FWHM are more inclined to have weaker packing density
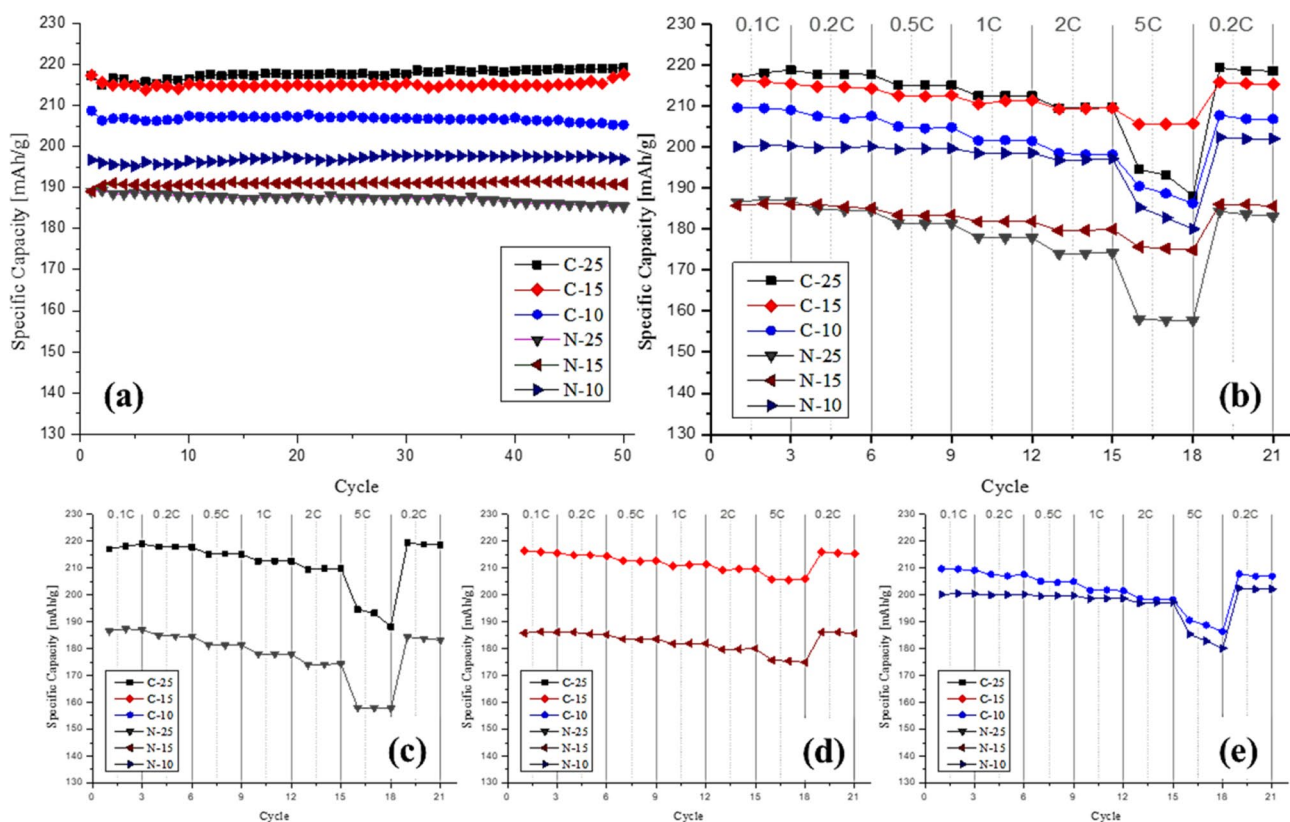
Fig. 7 Cycle performances of prepared samples (**a**), rate performances of prepared samples (**b**), **c** C-25 and N-25, **d** C-15 and N-15, **e** C-10 and N-10

Table 6 Rate performances of prepared samples

Name	0.1C	0.2C	0.5C	1C	2C	5C	0.2C*	2C/0.2C	5C/0.2C	0.2C*/0.2C
C-25	217.99	217.82	215.14	212.51	209.62	191.96	218.90	0.96	0.88	1.01
C-15	215.92	214.63	212.58	211.10	209.46	205.67	215.59	0.97	0.95	1.00
C-10	209.41	207.37	204.83	201.61	198.32	188.52	207.21	0.96	0.91	1.00
N-25	186.97	184.66	181.35	177.92	174.10	157.83	183.70	0.94	0.85	0.99
N-15	186.03	185.52	183.43	181.88	179.79	175.28	185.91	0.97	0.94	1.00
N-10	200.32	200.00	199.60	198.55	197.00	182.76	202.19	0.98	0.91	1.01

The specific capacity was assumed to 280 mAh/g for the 1 C-rate

0.2C*: After 5C cycle

Table 7 Powder resistivity of prepared samples and porosity of prepared anode

|	Conductivity vs porosity					
	N-25	N-15	N-5	C-25	C-15	C-5
Conductivity [S/cm]	91.63	70.60	66.68	41.46	37.84	24.14
Porosity (%)	30.76	33.72	41.90	35.05	36.91	42.68

[24–26]. In this experiment, FWHM decreased with decreasing particle size.

Coke samples with smaller particles have weaker electrical conductivity, which interferes with the transfer of electrons. At the same time, the increased porosity facilitates the diffusion of lithium ions. The charge/discharge of secondary batteries involves various simultaneous processes, such as electron transfer at electrodes and lithium diffusion in the electrolyte. As such, the most

Fig. 8 Powder resistivity and anode porosity comparison on the particle size of prepared samples
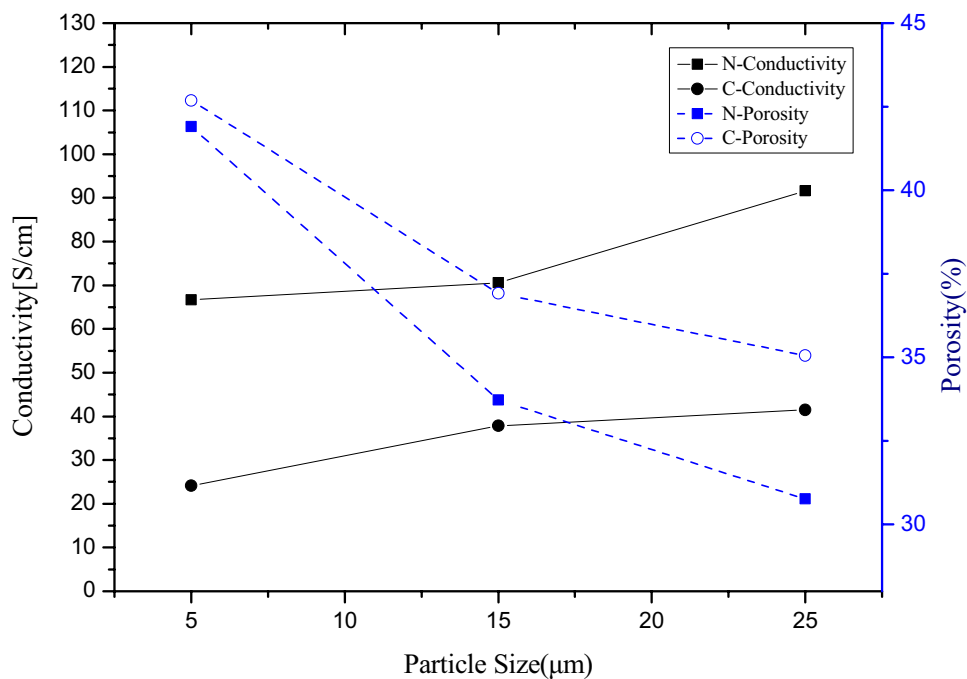
outstanding rate was achieved at the intersection of the two properties (particle size of 15 μm in Fig. 8).

4 Conclusion

This study examined the electrochemical performance in terms of crystallinity and particle properties (size and shape) of cokes.

The particles of pulverized coke varied in shape and size depending on crystallinity and orientation. Needle coke, which is characterized by high crystallinity and superior orientation, was pulverized in the form of plates; regular coke, having a more disordered orientation, was irregularly pulverized. SEI is more easily formed due to the irregular particles, and this lowers the initial efficiency.

Since materials with disordered orientation have increased capacity (Type III) in cavities between crystals, regular coke had a higher discharge capacity than that of needle coke. Given the rapid decrease in intercalation capacity (Type II) of materials having low crystallinity, both crystallinity and particle properties must be considered when fabricating anodic materials with high discharge capacity.

Rate performance is affected by both electron transfer properties (electrical conductivity) and the diffusion of lithium ions (porosity). For smaller particles, the increased contact resistance leads to a decrease in electrical conductivity. For larger particles, porosity decreases with enhanced packing density, and the rate of diffusion of lithium ions becomes slower. In this experiment, particles measuring 15 μm showed the most outstanding rate performance.

References

1. Park JK (2012) Principles and applications of lithium secondary batteries. Wiley-vch, Weinhenim
2. Kelly BT (1981) Physics of graphite. Applied Science, UK
3. Reynolds WN (1968) Physical properties of graphite. Elsevier, London
4. Song XY, Kinoshita K, Tran TD (1996) Microstructural characterization of lithiated graphite. J Electrochem Soc 143(6):L120
5. Endo M, Kim C, Nishimura K, Fujino T, Miyashita K (2000) Recent development of carbon materials for Li ion batteries. Carbon 38(2):183–197
6. Tamai H, Matsuoka S, Ishihara M, Yasuda H (2001) New carbon materials from pitch containing organotin compounds for anode of lithium ion batteries. Carbon 39(10):1515–1523
7. Lin Q, Zhang T, Bindra C, Fischer JE, Josefowicz JY (1997) Effect of morphology and texture on electrochemical properties of graphite anodes. J Power Sources 68(2):287–290
8. Sascha Z, Karin M (2006) Influence of nanomechanical crystal properties on the comminution process of particulate solids in spiral jet mills. Eur J Pharm Biopharm 62:194–201
9. Kawamura K, Bragg RH (1986) Graphitization of pitch coke: changes in mean interlayer spacing, strain and weight. Carbon 24:301–309
10. Hongyu W, Taisa I, Kenji F, Masaki Y (1999) Effect of milling on the electrochemical performance of natural graphite as an anode material for lithium-ion battery. J Power Sources 83(1–2):141–147
11. Luo L, Yao W, Liu J, Zhang H, Ma J, Jiang X (2019) The effect of the grinding process on pore structures, functional groups and release characteristic of flash pyrolysis of superfine pulverized coal. Fuel 235:1337–1346

12. Shafeeyan MS, Daud WMAW, Houshmand A, Shamiri A (2010) Review on surface modification of activated carbon for carbon dioxide adsorption. J Anal Appl Pyrol 89:143–151

13. Tuinstra F, Koenig JL (1970) Raman spectrum of graphite. J Chem Phys 53:1126–1130

14. Wang Y, Alsmeyer DC, McCreery RL (1990) Raman spectroscopy of carbon materials: structural basis of observed spectra. Chem Mater 2:557–563

15. Delhaes P, Couzi M, Trinquecoste M, Dentzer J, Hamidou H, Vix-GuterlA C (2006) A comparison between Raman spectroscopy and surface characterizations of multiwall carbon nanotubes. Carbon 44:3005–3013

16. Natarajan C, Fujimoto H, Mabuchi A, Tokumitsu K, Kasuh T (2001) Effect of mechanical milling of graphite powder on lithium intercalation properties. J Power Sources 92(1–2):187–192

17. Ku CH, Yoon SH, Korai Y (1998) Anodic performance and mechanism of mesophase-pitch-derived carbons in lithium ion batteries. J Power Sources 75(2):214–222

18. Mochida I, Ku CH, Korai Y (2001) Anodic performance and insertion mechanism of hard carbons prepared from synthetic isotropic pitches. Carbon 39:399–410

19. Stao K, Noguchi M, Demachi A, Oki N, Endo M (1994) A mechanism of lithium storage in disordered carbons. Science 264:556

20. Tastsumi K, Akai T, Imamura T, Zaghib K, Iwashita N, Higuchi S, Sawada Y (1996) ^{7}Li-nuclear magnetic resonance observation of lithium insertion into mesocarbon microbeads. J Electrochem Soc 143(6):1923

21. Guerard D, Herold A (1975) Intercalation of lithium into graphite and other carbons. Carbon 13(4):337–345

22. Habte BT, Jiang F (2018) Effect of microstructure morphology on Li-ion battery graphite anode performance: electrochemical impedance spectroscopy modeling and analysis. Solid State Ionics 314:81–91

23. Gruet D, Delobel B, Sicsic D, Lucas IT, Vivier V (2019) On the electrochemical impedance response of composite insertion electrodes—toward a better understanding of porous electrodes. Electrochim Acta 295:787–800

24. Thomas J, Fiske, Sudhir B, RailkarDilhanKalyon M (1994) Effects of segregation on the packing of spherical and nonspherical particles. Powder Technol 81(1):57–64

25. McGeary RK (1961) Mechanical packing of spherical particles. J Am Ceramic Soc 44(10):513–522

26. Kenneth W, Desmond ER (2014) Influence of particle size distribution on random close packing of spheres. Phy Rev. https://doi.org/10.1103/PhysRevE.90.022204